

CRiM-GS: Continuous Rigid Motion-Aware Gaussian Splatting from Motion-Blurred Images

Jungho Lee¹ Donghyeong Kim¹ Dogyoon Lee¹ Suhwan Cho¹ Minhyeok Lee¹ Sangyoun Lee¹

¹School of Electrical and Electronic Engineering, Yonsei University

{2015142131, 2donghyung87, nemotio, chosuhwan, hydragon516, syleee}@yonsei.ac.kr

<https://Jho-Yonsei.github.io/CRiM-Gaussian>

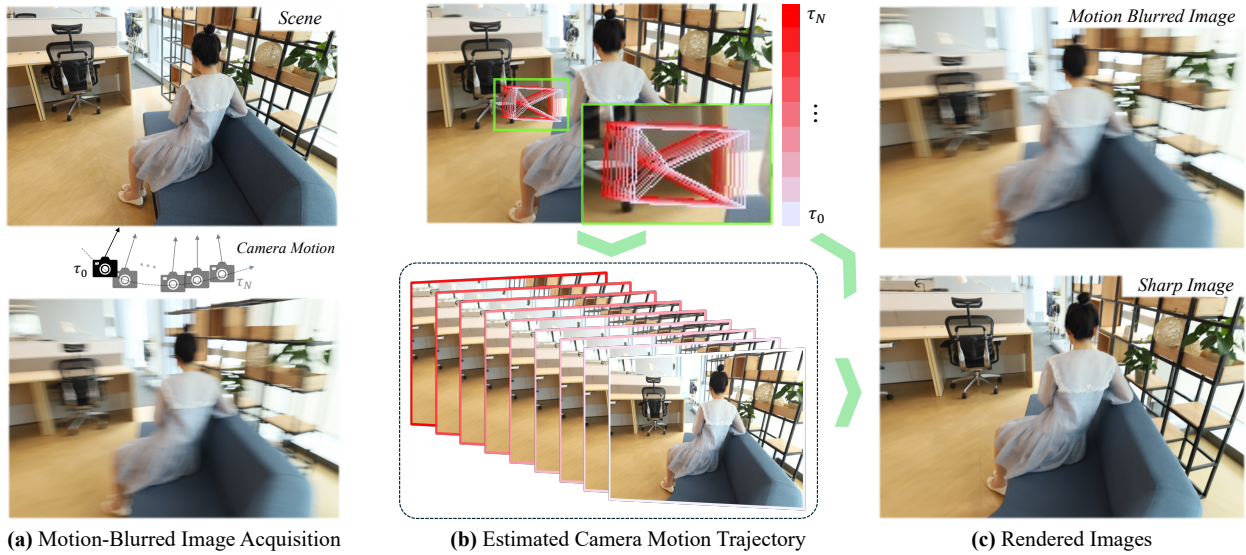


Figure 1. We propose CRiM-GS, a novel framework for reconstructing 3D scenes from camera motion-blurred images. (a) Camera motion-blurred images are generated by the continuous movement of the camera during the exposure time. (b) The top image represents the camera poses obtained through CRiM-GS, showing a continuous trajectory indicated by gradually changing colors. The bottom images are the rendering outputs from each camera pose. (c) By applying a weighted sum to the rendered images obtained in step (b), we get the motion-blurred output image shown at the top, while the sharp output image is rendered from the initial camera pose.

Abstract

3D Gaussian Splatting (3DGS) has gained significant attention for their high-quality novel view rendering, motivating research to address real-world challenges. A critical issue is the camera motion blur caused by movement during exposure, which hinders accurate 3D scene reconstruction. In this study, we propose CRiM-GS, a Continuous Rigid Motion-aware Gaussian Splatting that reconstructs precise 3D scenes from motion-blurred images while maintaining real-time rendering speed. Considering the complex motion patterns inherent in real-world camera movements, we predict continuous camera trajectories using neural ordinary differential equations (ODE). To ensure accurate modeling, we employ rigid body transformations with proper

regularization, preserving object shape and size. Additionally, we introduce an adaptive distortion-aware transformation to compensate for potential nonlinear distortions, such as rolling shutter effects, and unpredictable camera movements. By revisiting fundamental camera theory and leveraging advanced neural training techniques, we achieve precise modeling of continuous camera trajectories. Extensive experiments demonstrate state-of-the-art performance both quantitatively and qualitatively on benchmark datasets..

1. Introduction

Novel view synthesis has recently garnered significant attention, with neural radiance fields (NeRF) [27] making considerable advancements in photo-realistic neural render-

ing. NeRF takes sharp 2D images from multiple views as input to reconstruct precise 3D scenes, which are crucial for applications such as augmented reality (AR) and virtual reality (VR). NeRF models radiance and volume density through an implicit neural representation using multi-layer perceptrons (MLPs), based on the coordinates and viewing directions of 3D points. However, inefficient memory usage of this volume rendering process poses challenges for real-time applications. To address this, 3D Gaussian Splatting (3DGS) [15] has recently emerged, offering an alternative by explicitly representing 3D scenes and enabling high-quality real-time rendering through a differentiable splatting method.

However, for precise 3D scene representation in real-world scenarios, it is essential to address various forms of image quality degradation, such as camera motion blur and defocus blur. Current methods like NeRF and 3DGS rely on sharp images as input, which assumes highly ideal conditions. Obtaining such precise images requires a large depth of field (DoF), necessitating a very small aperture setting [11]. However, a smaller aperture limits light intake, leading to longer exposure times. With longer exposure, even slight camera movement introduces complex motion blur in the images. Therefore, developing techniques that can handle motion blur in input images is crucial for accurate 3D scene reconstruction. Our research tackles this challenge by focusing on reconstructing precise 3D scenes from images affected by camera motion blur, thus broadening the applicability of neural rendering in more realistic conditions.

Recently, several methods have been proposed to achieve sharp novel view rendering from camera motion-blurred images. Inspired by traditional blind image deblurring techniques, Deblur-NeRF [25] firstly introduces a method for deblurring 3D scenes. This approach designs a learnable kernel that intentionally blurs images during training, and during rendering, excludes the learned blurring kernel to render sharp novel view images. Following this approach, various methods targeting camera motion blur [17, 18, 35, 36, 51, 61] have emerged, aiming to improve blurring kernel estimation accuracy. However, all of these methods predict the camera trajectory without addressing for the continuity of camera motion throughout the exposure time (*e.g.*, simple spline function [51, 61]). While these approaches effectively model simple motion blur, they tend to oversmooth the trajectory in cases of complex camera motion.

In this paper, we propose a **Continuous Rigid Motion-aware Gaussian Splatting**, namely CRiM-GS, a novel approach with three key contributions. First, we apply neural ordinary differential equations (ODE) [5] to model continuous camera movement during exposure time, as illustrated in Fig. 1. By continuously modeling the camera trajectory in 3D space, we introduce a model that is fundamentally

different from existing methods [18, 25, 35, 51]. Second, inspired by Nerfies [31] and DP-NeRF [18], we incorporate rigid body transformations with explicit regularization, to accurately capture the shape and size of the static subject during camera movement. Third, to address potential non-linear distortions that can occur during fast camera motion, such as small rolling-shutter effects, we propose an adaptive distortion-aware transformation. This transformation softly refines the rigid body transformation with a higher degree of freedom. For superior rendering quality with real-time rendering speed, we employ Mip-Splatting [59], a differentiable rasterization-based method based on 3DGS [15], rather than ray tracing-based methods (*e.g.*, NeRF [27], TensoRF [4]). We evaluate and compare our approach on Deblur-NeRF [25] synthetic and real-world scene datasets, achieving state-of-the-art results across the benchmarks. To demonstrate the effectiveness of CRiM-GS, we conduct various ablative experiments on the proposed contributions.

2. Related Work

2.1. Neural Rendering

Neural rendering has seen explode in the fields of computer graphics and vision area thanks to the emergence of volumetric rendering and ray tracing-based neural radiance fields (NeRF) [27], which provide realistic rendering quality from 3D scenes. NeRF has led to a wide range of studies, including 3D mesh reconstruction [22, 46, 49, 50], dynamic scene [20, 21, 31, 32, 38, 47], and human avatars [14, 37, 53]. At the same time, several researches have aimed at overcoming slow rendering speed, such as TensoRF [4], Plenoxel [10], and Plenotree [58]. Among these advancements, the recent emergence of 3D Gaussian splatting (3DGS) [15], which offers remarkable performance along with fast training and rendering speed, has further accelerated research in the neural rendering. In addition to the aforementioned diverse scenarios for 3D scene modeling, there has been active research focusing on the external non-ideal conditions of given images, such as sparse-view images [29, 48, 55, 56], and the absence of camera parameters [2, 13, 52]. Moreover, there has been significant research attention on non-ideal conditions inherent to the images themselves, such as low-light [28, 34], blur [6, 18, 19, 25, 35, 36, 51, 61], and inconsistent appearance condition [26]. Recently, neural rendering from blurred images, which can occur during image acquisition, has attracted attention due to its practical applicability.

2.2. Neural Rendering from Blurry Images

Deblur-NeRF [25] firstly introduced the deblurred neural radiance fields by importing the blind-deblurring mechanism into the NeRF framework. They introduce specific blur kernel in front of the NeRF framework imitating the

blind deblurring in 2D image deblurring area. After the emergence of [25], several attempts have been proposed to model the precise blur kernel with various types of neural rendering baseline, such as TensorRF [4], and 3DGS [15]. DP-NeRF [18] proposes rigid blur kernel that predict the camera motion during image acquisition process as 3D rigid body motion to preserve the geometric consistency across the scene. BAD-NeRF [51] and BAD-Gaussians [61] similarly predict blur kernel as camera motions based on NeRF [27] and 3DGS [15], which assume the simple camera motion and interpolate them between predicted initial and final poses and design simple spline-based methods. PDRF [35] proposes progressive blur estimation model with hybrid 2-stage efficient rendering scheme that consists of coarse ray and fine voxel renderer. BAGS [36] proposes CNN-based multi-scale blur-agnostic degradation kernel with blur masking that indicates the blurred areas.

3. Preliminary

3.1. 3D Scene Blind Deblurring

For conventional image blind deblurring [3, 45, 54], the blurring kernel h is estimated without any supervision. The process to acquire blurry images is achieved by convolving h with sharp images, where the kernels for the convolution take a fixed grid of size around the pixel location p . Deblur-NeRF [25] applies this algorithm to NeRF [27], modeling an adaptive sparse kernel for 3D scene representation from blurry images. Deblur-NeRF acquires the blurry pixel color \mathbf{c}_{blur} by warping the original input ray into multiple rays that constitute the blur, then determining the pixel color from the colors obtained from these rays:

$$\mathbf{c}_{blur} = \sum_{i=0}^N w_p^i \mathbf{c}_p^i, \text{ w.r.t. } \sum_{i=0}^N w_p^i = 1, \quad (1)$$

where N and i respectively denote the number of warped rays for convolution and the corresponding index; w_p is the corresponding weight at each ray’s location, and \mathbf{c}_p represents the pixel color of sharp image. Deblur-NeRF enhances learning efficiency by setting the number of warped rays smaller than the kernel size of 2D convolution. In this paper, instead of warping rays, we propose a method to obtain blurry images by applying Eq. (1) to multiple rendered images.

3.2. 3D Gaussian Splatting

Unlike ray tracing-based methods [1, 4, 27], 3DGS [15] is built on a rasterization-based approach with differentiable 3D Gaussians. These 3D Gaussians are initialized from a sparse point cloud obtained via a Structure-from-Motion (SfM) [41, 43] algorithm and are defined as follows:

$$\mathbf{G}(\mathbf{x}) = e^{-\frac{1}{2}(\mathbf{x}-\boldsymbol{\mu})^\top \boldsymbol{\Sigma}^{-1}(\mathbf{x}-\boldsymbol{\mu})}, \quad (2)$$

where $\mathbf{x} \in \mathbb{R}^3$ is a point on the Gaussian \mathbf{G} centered at the mean vector $\boldsymbol{\mu} \in \mathbb{R}^3$ with an covariance matrix $\boldsymbol{\Sigma} \in \mathbb{R}^{3 \times 3}$. The 3D covariance matrix $\boldsymbol{\Sigma}$ is derived from a learnable scaling vector $\mathbf{s} \in \mathbb{R}^3$ and rotation quaternion $\mathbf{q} \in \mathbb{R}^4$, from which the scaling matrix $\mathbf{S} \in \mathbb{R}^{3 \times 3}$ and rotation matrix $\mathbf{R} \in \mathbb{R}^{3 \times 3}$ are obtained and represented as follows: $\boldsymbol{\Sigma} = \mathbf{R}\mathbf{S}\mathbf{S}^\top\mathbf{R}^\top$

For differentiable splatting [57], the Gaussians in the 3D world coordinate system are projected into the 2D camera coordinate system. This projection uses the viewing transformation $\mathbf{W} \in \mathbb{R}^{3 \times 3}$ and the Jacobian $\mathbf{J} \in \mathbb{R}^{2 \times 3}$ of the affined approximation of the projective transformation to derive the 2D covariance $\boldsymbol{\Sigma}^{2D} \in \mathbb{R}^{2 \times 2}$: $\boldsymbol{\Sigma}^{2D} = \mathbf{J}\mathbf{W}\boldsymbol{\Sigma}\mathbf{W}^\top\mathbf{J}^\top$

Each Gaussian includes a set of spherical harmonics (SH) coefficients and an opacity value α to represent view-dependent color \mathbf{c} . The pixel color \mathbf{c}_p is then obtained by applying alpha blending to \mathcal{N} ordered Gaussians:

$$\mathbf{c}_p = \sum_{i \in \mathcal{N}} \mathbf{c}_i \alpha_i \prod_{j=1}^{i-1} (1 - \alpha_j). \quad (3)$$

In this paper, we continuously model camera poses to project Gaussians \mathbf{G} onto the 2D camera coordinate system over the exposure time and obtain the final blurry image through a rasterization process of the obtained poses and the Gaussians.

3.3. Neural Ordinary Differential Equations

Neural ODE [5] is first proposed as an approach that interprets neural networks as the derivatives of a ODE systems, where ODE represents the dynamics inherent to the hidden states. Specifically, neural ODE are utilized to represent parameterized, time-continuous dynamics in the latent space, providing a unique solution given an initial value and numerical differential equation solvers [23]. Recently, there has been extensive research on neural ODE. For instance, Latent-ODE [40] models the continuous dynamics of irregularly sampled time-series data, while Vid-ODE [33] models a smooth latent space by capturing the underlying continuous dynamics of videos.

Neural ODE models a continuous and differentiable latent state $\mathbf{z}(\tau)$. Within an infinitesimally small step limit ϵ in the latent space, the local continuous dynamics are modeled as $\mathbf{z}(\tau + \epsilon) = \mathbf{z}(\tau) + \epsilon \cdot \frac{d\mathbf{z}(\tau)}{d\tau}$. The derivative of the latent state, $\frac{d\mathbf{z}(\tau)}{d\tau}$, is represented by a neural network $f(\mathbf{z}(\tau), \tau; \phi)$ parameterized by learnable parameters ϕ . The latent state at any arbitrary time τ_s is obtained by solving the ODE from the initial time τ_0 :

$$\mathbf{z}(\tau_s) = \mathbf{z}(\tau_0) + \int_{\tau_0}^{\tau_s} f(\mathbf{z}(\tau), \tau; \phi) d\tau. \quad (4)$$

The simplest method to solve ODE is the Euler method [9], which is a fixed-step-size first-order solver. Additionally,

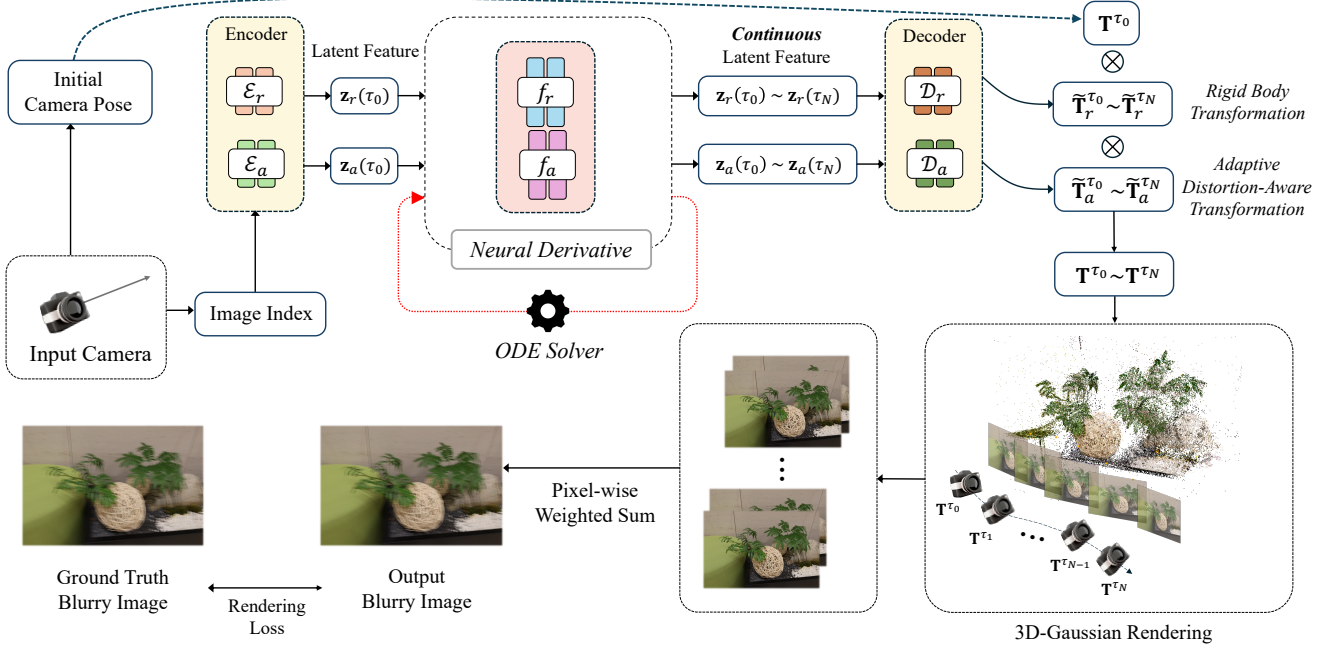


Figure 2. Pipeline of CRiM-GS. The input camera contains the image index and the initial camera pose information. CRiM-GS iteratively solves the ODE using the encoded image index and the neural derivative presented in Sec. 4.2 and Sec. 4.3, and obtains N transformed camera poses after decoding. Then, N images are rendered through 3DGS, and a blurry image is obtained through the pixel-wise weighted-sum presented in Sec. 4.4

the Runge-Kutta [16] methods are preferred as a higher-order solvers as they offer enhanced convergence and stability.

The derivative f modeled by the neural network is expressed as a uniformly Lipschitz continuous non-linear function in \mathbf{z} and τ [12]. Therefore, the solution obtained through the solver for any given integration interval (τ_i, τ_j) is always unique in the integration of the continuous dynamics. We model the non-linear 3D camera trajectory as time-continuous using neural ODE in the latent space to ensure a continuous representation. In our experiments, we adopt the Dormand-Prince-Shampine fifth-order [8] Runge-Kutta solver for all experiments, following [5].

4. Method

4.1. CRiM-GS Framework

Our goal is to reconstruct a sharp 3D scene using only camera motion-blurred images as input, thereby obtaining deblurred novel view images. Inspired by image blind deblurring methods, we follow the approach of DeblurNeRF [25], learning a kernel that intentionally blurs images and excluding this kernel during rendering to produce sharp images. As illustrated in Fig. 1, our blurring process consists of camera poses along the camera motion trajectory, generated continuously in time order through neural

ODE [5]. Each pose is composed of a rigid body transformation $\mathbf{T}_r = [\mathbf{R}_r | \mathbf{t}_r]$ (Sec. 4.2), which maintains the shape and size of the subject, and an adaptive-distortion aware transformation $\mathbf{T}_a = [\mathbf{R}_a | \mathbf{t}_a]$ (Sec. 4.3), which accounts for nonlinear distortions such as small rolling-shutter effect. Rigid body transformation exists in a dense $SE(3)$ space, whereas adaptive distortion-aware transformation introduces slight deviations to better capture such distortions while remaining close to $SE(3)$. Note that $\mathbf{R} \in \mathbb{R}^{3 \times 3}$ and $\mathbf{t} \in \mathbb{R}^3$ represent rotation matrix and translation vector, and $\tilde{\mathbf{R}} \in \mathbb{R}^{3 \times 3}$ and $\tilde{\mathbf{t}} \in \mathbb{R}^3$ stand for multiplicative offsets of change of the rotation matrix and translation vector, respectively. Given the two transformation matrices $\tilde{\mathbf{T}}_r = [\tilde{\mathbf{R}}_r | \tilde{\mathbf{t}}_r]$ and $\tilde{\mathbf{T}}_a = [\tilde{\mathbf{R}}_a | \tilde{\mathbf{t}}_a]$, the subsequent pose \mathbf{T}^{τ_s} in the camera motion is derived as follows:

$$\mathbf{T}^{\tau_s} = \mathbf{T}^{\tau_0} \tilde{\mathbf{T}}_r^{\tau_s} \tilde{\mathbf{T}}_a^{\tau_s}, \text{ where } \mathbf{T} = [\mathbf{R} | \mathbf{t}] = \begin{bmatrix} \mathbf{R} & \mathbf{t} \\ 0 & 1 \end{bmatrix}, \quad (5)$$

where $\mathbf{T}^{\tau_0} = [\mathbf{R}^{\tau_0} | \mathbf{t}^{\tau_0}]$ and $\mathbf{T}^{\tau_s} = [\mathbf{R}^{\tau_s} | \mathbf{t}^{\tau_s}]$ denote the camera poses at the initial state and the time τ_s . By rendering N images from the obtained N camera poses and computing their pixel-wise weighted sum (Sec. 4.4), we obtain the final blurred image. Our framework is shown in Fig. 2.

4.2. Continuous Rigid Body Motion

To design the camera motion trajectory within the exposure time, we apply rigid body transformation in that the shape and size of the object remain unchanged. Rigid body transformation requires three components for the unit screw axis $\mathcal{S} = (\hat{\omega}, v)$: the unit rotation axis $\hat{\omega} \in \mathbb{R}^3$, the rotation angle θ about the axis, and the translation component $v \in \mathbb{R}^3$ for translation. Considering that the direction and extent of blur vary for each image in a single scene, we embed the image index of the scene to obtain different embedded features for each image as shown in Fig. 2. These features are then passed through an encoder \mathcal{E}_r with a single-layer MLP, transforming them into the latent features $\mathbf{z}_r(\tau_0)$, which potentially represent for $\hat{\omega}$, θ , and v of \mathcal{S} . Then, we model the continuous latent space for the screw axis using a neural ODE [5] to assign the latent continuity to the screw axis in camera motion trajectory. The neural derivative f of the latent features for the screw axis is expressed as $\frac{d\mathbf{z}_r(\tau)}{d\tau} = f(\mathbf{z}_r(\tau), \tau; \phi)$, and the latent features at an arbitrary time τ_s can be obtained by ODE solver, numerically integrating f from τ_0 to τ_s :

$$\mathbf{z}_r(\tau_s) = \mathbf{z}_r(\tau_0) + \int_{\tau_0}^{\tau_s} f(\mathbf{z}_r(\tau), \tau; \phi) d\tau. \quad (6)$$

To obtain N poses along the camera trajectory, we uniformly sample N time points within the fixed exposure time and get N latent features by applying the Eq. (6) to them. We then transform the latent features obtained by the ODE solver into the unit screw axis \mathcal{S} using a single-layer MLP decoder \mathcal{D}_r . In Nerfies [31] and DP-NeRF [18], the angular velocity $\omega = \hat{\omega}\theta$ is modeled and then decomposed into the unit rotation axis $\hat{\omega}$ and the rotation angle θ , making the two elements dependent on each other. However, since θ represents the rotation amount about the axis, these two elements should be independent. Therefore, we model $\hat{\omega}$ with normalization and θ independently through the decoder \mathcal{D}_r :

$$\mathcal{D}_r(\mathbf{z}_r(\tau)) = (\hat{\omega}^\tau, \theta^\tau, v^\tau), \text{ where } \|\hat{\omega}^\tau\| = 1. \quad (7)$$

According to [24], the screw axis $\mathcal{S}^\tau = (\hat{\omega}^\tau, v^\tau)$ is a normalized twist, so the infinitesimal transformation matrix $[\mathcal{S}^\tau] \in \mathbb{R}^{4 \times 4}$ is represented as follows:

$$[\mathcal{S}^\tau] = \begin{bmatrix} [\hat{\omega}^\tau] & v^\tau \\ 0 & 0 \end{bmatrix} \in \mathfrak{se}(3), \quad (8)$$

where $[\hat{\omega}^\tau] \in \mathfrak{so}(3)$ is a 3×3 skew-symmetric matrix of vector $\hat{\omega}^\tau$. To derive the infinitesimal transformation matrix $[\mathcal{S}^\tau]\theta^\tau \in \mathfrak{se}(3)$ on the Lie algebra to the transformation matrix $\mathbf{T}_r^\tau \in SE(3)$ in the Lie group, we use the matrix exponential $e^{[\mathcal{S}^\tau]\theta^\tau}$, whose rotation matrix and translation vector are $\mathbf{R}_r^\tau = e^{[\hat{\omega}^\tau]\theta^\tau}$ and $\mathbf{t}_r^\tau = G(\theta^\tau)v^\tau$, respectively. These matrices are expressed as follows using Rodrigues'

formula [39] through Taylor expansion:

$$e^{[\hat{\omega}^\tau]\theta^\tau} = I + \sin \theta^\tau [\hat{\omega}^\tau] + (1 - \cos \theta^\tau) [\hat{\omega}^\tau]^2 \in SO(3), \quad (9)$$

$$G(\theta^\tau) = I\theta^\tau + (1 - \cos \theta^\tau) [\hat{\omega}^\tau] + (\theta^\tau - \sin \theta^\tau) [\hat{\omega}^\tau]^2. \quad (10)$$

Through the whole process, we obtain N continuous rigid body transformation matrices $\mathbf{T}_r = e^{[\mathcal{S}]\theta}$, and by multiplying these with the input pose as in Eq. (5), we obtain the transformed poses. We show whole derivation process of Eqs. (9) and (10) in the **appendix**, referring the Modern Robotics [24].

4.3. Adaptive Distortion-Aware Transformation

In real-world scenarios, blurry images captured with fast camera motion may exhibit nonlinear distortions, such as small rolling shutter effects, which are present but challenging to detect visually. Consequently, such distortions may not be fully addressed by rigid body transformations alone, suggesting the need for more sophisticated models to accurately handle these complexities. Based on this issue, we propose an adaptive distortion-aware transformation to provide additional refinement to the rigid body transformation. This transformation has higher degrees of freedom from a learning perspective and is simple to implement. The adaptive distortion-aware transformation optimizes the transformation matrix close to $SE(3)$ directly without any screw axis components as described in Eq. (8). Thus, instead of modeling $\hat{\omega}$ and v , this transformation designs a matrix $\tilde{\mathbf{R}}_a$ which is regularized close to rotation matrix, and the translation vector $\tilde{\mathbf{t}}_a$. This process begins by encoding the image index into the latent state $\mathbf{z}_a(\tau_0)$ of $\tilde{\mathbf{R}}_a$ and $\tilde{\mathbf{t}}_a$ using the encoder \mathcal{E}_a with a single-layer MLP, similar to Sec. 4.2. The latent state $\mathbf{z}_a(\tau_s)$ at any arbitrary time τ_s is obtained using the neural derivative g parameterized by ψ and a solver:

$$\mathbf{z}_a(\tau_s) = \mathbf{z}_a(\tau_0) + \int_{\tau_0}^{\tau_s} g(\mathbf{z}_a(\tau), \tau; \psi) d\tau. \quad (11)$$

The latent features are then decoded into rotation matrix component \mathbf{A}_a^τ and translation vector $\tilde{\mathbf{t}}_a^\tau$ through a single-layer MLP decoder \mathcal{D}_a :

$$\mathcal{D}_a(\mathbf{z}_a(\tau)) = (\mathbf{A}_a^\tau, \tilde{\mathbf{t}}^\tau) \rightarrow \tilde{\mathbf{T}}_a^\tau = \begin{bmatrix} \tilde{\mathbf{R}}_a^\tau & \tilde{\mathbf{t}}_a^\tau \\ 0 & 1 \end{bmatrix}, \quad (12)$$

where $\tilde{\mathbf{R}}_a^\tau = \mathbf{A}_a^\tau + \mathbf{I}$ and \mathbf{I} is the identity matrix to initialize $\tilde{\mathbf{R}}_a^\tau$ to identity transformation. Since the adaptive distortion-aware transformation is intended to softly refine the rigid body transformation, it should not significantly affect the rigid body transformation during the initial stages of training. Therefore, we initialize the weights of the decoder to approximate \mathbf{A}_a^τ to zero matrix using a uniform distribution $\mathcal{U}(-10^{-5}, 10^{-5})$, which means that $\tilde{\mathbf{R}}_a^\tau$ is initialized close to identity matrix. Furthermore, for

modeling the transformation matrix $\tilde{\mathbf{T}}_a^\tau$ to approximate the main conditions of the $SE(3)$ space, we introduce a simple regularization loss. The proposed loss is \mathcal{L}_o , which ensures the orthogonality condition of rotation matrix: $\mathcal{L}_o = \|\tilde{\mathbf{R}}_a^\top \tilde{\mathbf{R}}_a - \mathbf{I}\|_2$. This regularization ensures that the transformation matrix $\tilde{\mathbf{T}}_a$ closely lies within the $SE(3)$ space. Note that this transformation should not be perfectly in the $SE(3)$ space as it aims to compensate the subtle distortions during camera motion. Finally, we apply Eq. (6) using $\tilde{\mathbf{T}}_a^{\tau_s}$ and $\tilde{\mathbf{T}}_r^{\tau_s}$ obtained from Sec. 4.2 to get the refined transformed camera pose \mathbf{T}^{τ_s} . We discuss the relationships between the adaptive distortion-aware transformation and image distortion from camera motion blur in Sec. 5.4.

4.4. Optimization

Pixel-wise Weight. Once the N images along the camera motion trajectory are obtained from the N camera poses, we apply a pixel-wise weighted sum to create the blurry image \mathcal{I}_{blur} , following previous research [18, 19, 25, 35]. To satisfy Eq. (1), we use a shallow CNN \mathcal{F} and a softmax function to compute the pixel-wise weights $\mathcal{P} \in \mathbb{R}^{N \times H \times W \times 3}$ for the resulting images, as follows:

$$\mathcal{I}_{blur} = \sum_{i=1}^N \mathcal{I}^{\tau_i} \cdot \mathcal{P}^{\tau_i}, \text{ where } \mathcal{P} = \text{softmax}(\mathcal{F}(\mathcal{I})), \quad (13)$$

where \mathcal{I}^{τ_i} is the i -th image along the camera motion, and \mathcal{P}^{τ_i} is the pixel-wise weight of i -th image. Additionally, we adopt per-pixel scalar mask [36] $\mathcal{M} \in \mathbb{R}^{H \times W \times 3}$ to generate final output blurry image \mathcal{I}_{out} by blending the sharp image \mathcal{I}^{τ_0} at camera pose \mathbf{T}^{τ_0} and the blurry image \mathcal{I}_{blur} acquired by pixel-wise weight: $\mathcal{I}_{out} = (1 - \mathcal{M}) \cdot \mathcal{I}^{\tau_0} + \mathcal{M} \cdot \mathcal{I}_{blur}$. The scalar mask aims to decide whether each pixel is blurry or not, and a small sparsity constraint is applied to the mask to assign a larger weight on \mathcal{I}^{τ_0} , namely mask sparsity loss [36] $\mathcal{L}_{\mathcal{M}}$, which is a mean value of the scalar mask. This method allows us to obtain the final precise blurry image, which is then optimized against the ground truth blurry image.

Objective. We optimize the learning process using the \mathcal{L}_1 loss and D-SSIM between the generated output blurry image \mathcal{I}_{out} and the ground truth blurry image, similar to 3D-GS [15]. The \mathcal{L}_1 loss ensures pixel-wise accuracy, while D-SSIM captures perceptual differences. Additionally, we apply the regularization loss \mathcal{L}_o (Sec. 4.3) to regularize the calibration-enhanced transformation and mask sparsity loss $\mathcal{L}_{\mathcal{M}}$. The final objective \mathcal{L} is defined as follows:

$$\mathcal{L} = (1 - \lambda_c)\mathcal{L}_1 + \lambda_c\mathcal{L}_{D-SSIM} + \lambda_o\mathcal{L}_o + \lambda_{\mathcal{M}}\mathcal{L}_{\mathcal{M}}, \quad (14)$$

where λ_c is a factor for balancing \mathcal{L}_1 and \mathcal{L}_{D-SSIM} , and λ_o and $\lambda_{\mathcal{M}}$ are factors for \mathcal{L}_o and $\mathcal{L}_{\mathcal{M}}$, respectively.

Table 1. Comparisons on synthetic and real-world scene dataset. “*” denotes the results obtained by reproducing the released code. The orange and yellow cells respectively indicate the highest and second-highest value.

Methods	Synthetic Scene			Real-World Scene		
	PSNR↑	SSIM↑	LPIPS↓	PSNR↑	SSIM↑	LPIPS↓
Naive NeRF [27]	23.78	0.6807	0.3362	22.69	0.6347	0.3687
NeRF+MPR [60]	25.11	0.7476	0.2148	23.38	0.6655	0.3140
Deblur-NeRF [25]	28.77	0.8593	0.1400	25.63	0.7645	0.1820
PDRF-10* [35]	28.86	0.8795	0.1139	25.90	0.7734	0.1825
BAD-NeRF* [51]	27.32	0.8178	0.1127	22.82	0.6315	0.2887
DP-NeRF [18]	29.23	0.8674	0.1184	25.91	0.7751	0.1602
DeblurGS* [30]	20.22	0.5454	0.1042	20.48	0.5813	0.1186
BAD-Gaussians* [61]	21.12	0.5852	0.1007	20.82	0.5917	0.1000
Deblurring 3DGS [17]	28.24	0.8580	0.1051	26.61	0.8224	0.1096
BAGS [36]	27.34	0.8353	0.1116	26.70	0.8237	0.0956
CRiM-GS	30.46	0.9095	0.0441	27.35	0.8315	0.0633

5. Experiments

Datasets. CRiM-GS is evaluated using the camera motion blur dataset provided by Deblur-NeRF [25], which includes 5 synthetic scenes and 10 real-world scenes. The synthetic scenes are generated using Blender [7], and each single image that constitutes a motion-blurred image is obtained through linear interpolation between the first and last camera poses along the camera path. The obtained images are combined in linear RGB space to create the final blurred images. The real-world scenes consist of images captured with a CANON EOS RP camera, where the exposure time is manually set to produce blurry images. For each scene, all images exhibit different types of blur, including non-uniform blur. We obtain the camera poses for each image and the initial point clouds for training the Gaussian primitives by applying COLMAP [41, 43]. We run COLMAP with blurry images for synthetic and real-world scenes.

5.1. Novel View Synthesis Results

For quantitative results, we evaluate CRiM-GS using three metrics: peak signal-to-noise ratio (PSNR), structural similarity index measure (SSIM), and learned perceptual image patch similarity (LPIPS). We compare our method with both ray-based and rasterization methods. Note that the results for BAD-GS [61] are obtained by re-running the released code ourselves. The overall results for all scenes are shown in Tab. 1, demonstrating that our method achieves superior performance compared to all other methods. Specifically for the LPIPS, CRiM-GS shows an improvement of approximately 52% for synthetic scenes and 33% for real-world scenes than the state-of-the-art, and the best LPIPS performance across all scenes not only for synthetic dataset but also real-world dataset. Additionally, benefiting from using Mip-Splatting [59] as our backbone, our proposed method ensures fast training and rendering speeds. Although BAD-

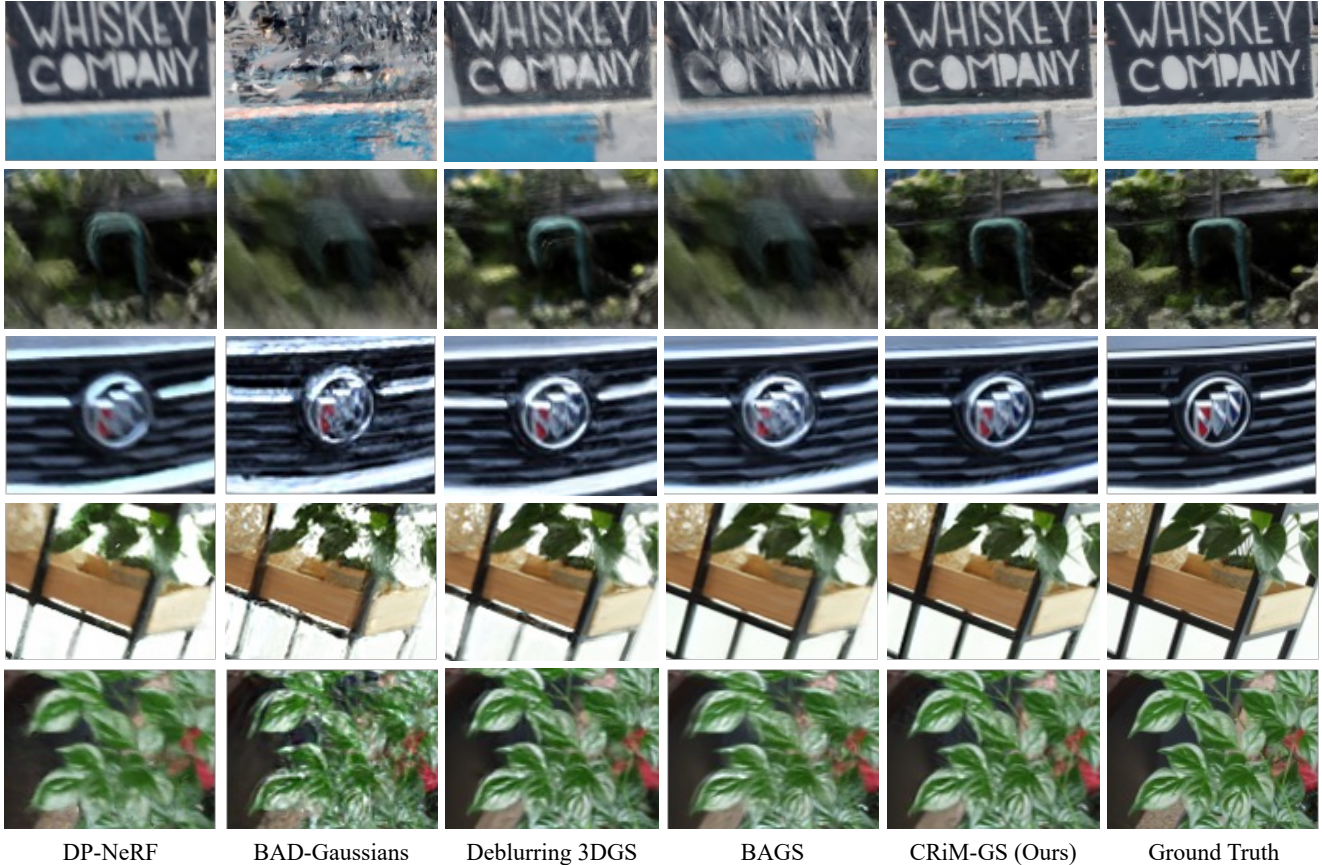


Figure 3. Qualitative comparison on the synthetic and real-world scenes.

Table 2. Comparisons on synthetic and real-world dataset. We evaluate the performance on three metrics (PSNR, SSIM, LPIPS).

Methods	Synthetic Scene			Real-World Scene		
	PSNR \uparrow	SSIM \uparrow	LPIPS \downarrow	PSNR \uparrow	SSIM \uparrow	LPIPS \downarrow
Baseline [59]	21.09	0.5974	0.2774	21.80	0.6135	0.2698
CRiM-GS						
(A) with $\tilde{\mathbf{T}}_r$	26.38	0.8355	0.0859	25.29	0.7833	0.0985
(B) with $\tilde{\mathbf{T}}_r + \mathcal{P}$	29.66	0.8918	0.0546	26.77	0.8124	0.0778
(C) with $\tilde{\mathbf{T}}_a$	25.80	0.8271	0.1052	25.09	0.7752	0.1082
(D) with $\tilde{\mathbf{T}}_a + \mathcal{P}$	28.79	0.8714	0.0833	26.56	0.8070	0.0906
(E) with $\tilde{\mathbf{T}}_r + \tilde{\mathbf{T}}_a$	27.38	0.8449	0.0762	25.52	0.7882	0.0973
(F) with $\tilde{\mathbf{T}}_r + \tilde{\mathbf{T}}_a + \mathcal{P}$	30.46	0.9095	0.0441	27.35	0.8315	0.0633

GS [61] achieves relatively good LPIPS scores, their PSNR and SSIM scores are lower, indicating that their camera poses are not properly optimized. More details about pose optimization are in the **appendix**.

To qualitatively evaluate the results, we visualize rendering results of several scenes and compare to other methods as shown in Fig. 3. These include two synthetic scene and three real-world scenes. Our method shows superior qualitative results compared to the state-of-the-art ray-based

method DP-NeRF [18], as well as rasterization-based methods such as BAD-GS [61], BAGS [36], and Deblurring 3DGS [17]. The lowest row of Fig. 3 stands for visualization of PARTERRE scene, which shows slightly lower PSNR and SSIM than Deblurring 3DGS, but shows better qualitative performance with well-detailed leaves.

5.2. Ablation Study

As shown in Sec. 5.1, to thoroughly demonstrate the validity and effectiveness of our contributions, we conduct ablation experiments on all scenes, not just a single scene.

Ablation on Continuous Transformation. Referring Sec. 5.1, the model (A) with the main component of CRiM-GS, the continuous rigid body transformation, shows a significant performance increase, indicating that the camera motion path is well-modeled. The model (C) with only the adaptive distortion-aware transformation performs worse than the model with only the rigid body transformation, suggesting that the adaptive distortion-aware transformation leads to suboptimal results due to its too high degrees of freedom. Therefore, the model (E) combining both transformations, which refines camera motion distortion, achieves



Figure 4. Camera Trajectory Visualization. Red cones stand for camera poses, and the images below are the output blurry images.

the best performance without pixel-wise weights.

Ablation on Pixel-wise Weight. The pixel-wise weight, inspired by traditional ray-based 3D scene deblurring methods [18, 25, 36] and blind image deblurring methods [44, 60], differs from the approach of averaging images that constitute a blurry image. As shown in Sec. 5.1 for models (B), (D), and (F), applying this method consistently results in higher performance than not applying it. This indicates that by assigning corresponding weights to each pixel location, a more precise blurred image is reconstructed, and the images that constitute the blurry image are modeled more accurately, surpassing existing state-of-the-art methods.

5.3. Camera Trajectory Visualization

We visualize the continuous camera trajectories for the HERON and STAIR scenes from the Deblur-NeRF Real-World dataset, as shown in Fig. 4. The camera trajectory for a single motion-blurred image is represented by colored cones, with the cone’s color gradually transitioning from red to light purple as time progresses from t_0 to t_N . The visualized trajectories confirm that the camera paths generated by CRiM-GS are smoothly continuous, validating that the continuous transformations described in Secs. 4.2 and 4.3 function as intended. Additionally, the output blurry images in Fig. 4 align with the visualized camera poses, accurately reflecting both the positions and directions of the camera. Specifically, even though the camera path in the HERON scene on the left is nonlinear, CRiM-GS accurately predicts this path and generates a precise blurry image.

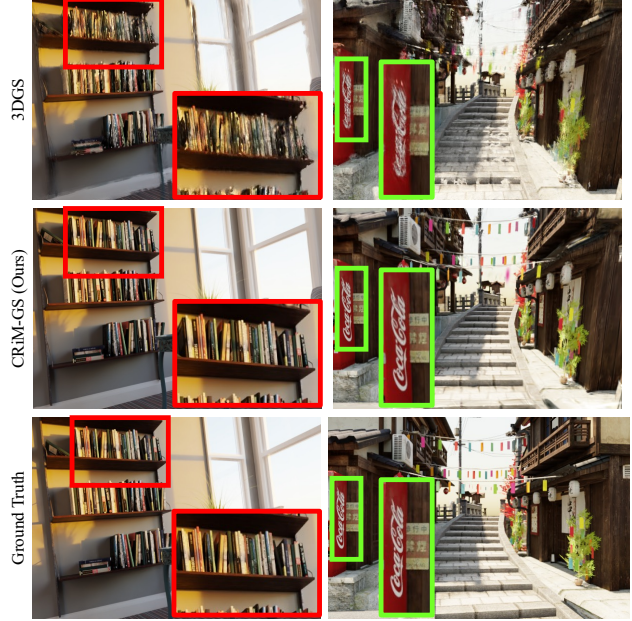


Figure 5. Rendering Results on Rolling Shutter Effect Dataset [42]

5.4. Rolling Shutter Effect Compensation

To demonstrate the effectiveness of the adaptive distortion-aware transformation in correcting nonlinear distortions, we conducted experiments on a dataset with rolling shutter effects [42]. As shown in Fig. 5, while 3DGS [15] suffers from significant geometric distortions, our method produces results closely matching the ground truth. This capability stems from the inherent flexibility of the adaptive distortion-aware transformation, which can accommodate both linear transformations such as affine transformations and nonlinear ones such as deformable transformations. Thus, as shown in Sec. 5.1, combining our proposed transformation with rigid body transformations improves performance by addressing the subtle distortions present in motion-blurred images, effectively enhancing the accuracy of the results.

6. Conclusion

We propose CRiM-GS, a novel method for reconstructing sharp 3D scenes from blurry images caused by camera motion. Under the assumption that objects remain static during camera movement, we introduce a rigid body transformation method and further enhance it with an adaptive distortion-aware transformation to correct potential real-world distortions. These transformations are continuously modeled using neural ODE in 3D physical space, capturing continuous camera motion trajectories. Drawing inspiration from traditional image deblurring techniques and prior 3D scene deblurring research, we incorporate a pixel-wise weighting strategy with a lightweight CNN. CRiM-GS surpasses state-of-the-art

methods in 3D scene deblurring, with extensive experiments validating the effectiveness of each component.

References

- [1] Jonathan T Barron, Ben Mildenhall, Matthew Tancik, Peter Hedman, Ricardo Martin-Brualla, and Pratul P Srinivasan. Mip-nerf: A multiscale representation for anti-aliasing neural radiance fields. In *Proceedings of the IEEE/CVF International Conference on Computer Vision*, pages 5855–5864, 2021. [3](#)
- [2] Wenjing Bian, Zirui Wang, Kejie Li, Jia-Wang Bian, and Victor Adrian Prisacariu. Nope-nerf: Optimising neural radiance field with no pose prior. In *Proceedings of the IEEE/CVF Conference on Computer Vision and Pattern Recognition*, pages 4160–4169, 2023. [2](#)
- [3] Ayan Chakrabarti. A neural approach to blind motion deblurring. In *Computer Vision—ECCV 2016: 14th European Conference, Amsterdam, The Netherlands, October 11–14, 2016, Proceedings, Part III 14*, pages 221–235. Springer, 2016. [3](#)
- [4] Anpei Chen, Zexiang Xu, Andreas Geiger, Jingyi Yu, and Hao Su. Tensorf: Tensorial radiance fields. In *European Conference on Computer Vision*, pages 333–350. Springer, 2022. [2](#), [3](#), [13](#)
- [5] Ricky TQ Chen, Yulia Rubanova, Jesse Bettencourt, and David K Duvenaud. Neural ordinary differential equations. *Advances in neural information processing systems*, 31, 2018. [2](#), [3](#), [4](#), [5](#), [12](#)
- [6] Wenbo Chen and Ligang Liu. Deblur-gs: 3d gaussian splatting from camera motion blurred images. *Proceedings of the ACM on Computer Graphics and Interactive Techniques*, 7(1):1–15, 2024. [2](#)
- [7] Blender Online Community. *Blender - a 3D modelling and rendering package*. Blender Foundation, Stichting Blender Foundation, Amsterdam, 2018. [6](#)
- [8] John R Dormand and Peter J Prince. A family of embedded runge-kutta formulae. *Journal of computational and applied mathematics*, 6(1):19–26, 1980. [4](#)
- [9] Leonhard Euler. *Institutionum calculi integralis*. impensis Academiae imperialis scientiarum, 1845. [3](#)
- [10] Sara Fridovich-Keil, Alex Yu, Matthew Tancik, Qinhong Chen, Benjamin Recht, and Angjoo Kanazawa. Plenoxels: Radiance fields without neural networks. In *Proceedings of the IEEE/CVF Conference on Computer Vision and Pattern Recognition*, pages 5501–5510, 2022. [2](#)
- [11] Eugene Hecht. *Optics*. Pearson Education India, 2012. [2](#)
- [12] Edward L Ince. *Ordinary differential equations*. Courier Corporation, 1956. [4](#)
- [13] Yoonwoo Jeong, Seokjun Ahn, Christopher Choy, Anima Anandkumar, Minsu Cho, and Jaesik Park. Self-calibrating neural radiance fields. In *Proceedings of the IEEE/CVF International Conference on Computer Vision*, pages 5846–5854, 2021. [2](#)
- [14] Wei Jiang, Kwang Moo Yi, Golnoosh Samei, Oncel Tuzel, and Anurag Ranjan. Neuman: Neural human radiance field from a single video. In *European Conference on Computer Vision*, pages 402–418. Springer, 2022. [2](#)
- [15] Bernhard Kerbl, Georgios Kopanas, Thomas Leimkühler, and George Drettakis. 3d gaussian splatting for real-time radiance field rendering. *ACM Transactions on Graphics*, 42(4):1–14, 2023. [2](#), [3](#), [6](#), [8](#), [13](#)
- [16] Wilhelm Kutta. *Beitrag zur näherungsweise Integration totaler Differentialgleichungen*. Teubner, 1901. [4](#)
- [17] Byeonghyeon Lee, Howoong Lee, Xiangyu Sun, Usman Ali, and Eunbyung Park. Deblurring 3d gaussian splatting. *arXiv preprint arXiv:2401.00834*, 2024. [2](#), [6](#), [7](#), [16](#)
- [18] Dogyoon Lee, Minhyeok Lee, Chajin Shin, and Sangyoun Lee. Dp-nerf: Deblurred neural radiance field with physical scene priors. In *Proceedings of the IEEE/CVF Conference on Computer Vision and Pattern Recognition*, pages 12386–12396, 2023. [2](#), [3](#), [5](#), [6](#), [7](#), [8](#), [16](#)
- [19] Jungho Lee, Dogyoon Lee, Minhyeok Lee, Donghyung Kim, and Sangyoun Lee. Smurf: Continuous dynamics for motion-deblurring radiance fields. *arXiv preprint arXiv:2403.07547*, 2024. [2](#), [6](#), [13](#)
- [20] Tianye Li, Mira Slavcheva, Michael Zollhoefer, Simon Green, Christoph Lassner, Changil Kim, Tanner Schmidt, Steven Lovegrove, Michael Goesele, Richard Newcombe, et al. Neural 3d video synthesis from multi-view video. In *Proceedings of the IEEE/CVF Conference on Computer Vision and Pattern Recognition*, pages 5521–5531, 2022. [2](#)
- [21] Zhengqi Li, Simon Niklaus, Noah Snavely, and Oliver Wang. Neural scene flow fields for space-time view synthesis of dynamic scenes. In *Proceedings of the IEEE/CVF Conference on Computer Vision and Pattern Recognition*, pages 6498–6508, 2021. [2](#)
- [22] Zhaoshuo Li, Thomas Müller, Alex Evans, Russell H Taylor, Mathias Unberath, Ming-Yu Liu, and Chen-Hsuan Lin. Neuralangelo: High-fidelity neural surface reconstruction. In *Proceedings of the IEEE/CVF Conference on Computer Vision and Pattern Recognition*, pages 8456–8465, 2023. [2](#)
- [23] Ernest Lindelöf. Sur l’application de la méthode des approximations successives aux équations différentielles ordinaires du premier ordre. *Comptes rendus hebdomadaires des séances de l’Académie des sciences*, 116(3):454–457, 1894. [3](#)
- [24] Kevin M Lynch and Frank C Park. *Modern robotics*. Cambridge University Press, 2017. [5](#), [14](#)
- [25] Li Ma, Xiaoyu Li, Jing Liao, Qi Zhang, Xuan Wang, Jue Wang, and Pedro V Sander. Deblur-nerf: Neural radiance fields from blurry images. In *Proceedings of the IEEE/CVF Conference on Computer Vision and Pattern Recognition*, pages 12861–12870, 2022. [2](#), [3](#), [4](#), [6](#), [8](#), [16](#)
- [26] Ricardo Martin-Brualla, Noha Radwan, Mehdi SM Sajjadi, Jonathan T Barron, Alexey Dosovitskiy, and Daniel Duckworth. Nerf in the wild: Neural radiance fields for unconstrained photo collections. In *Proceedings of the IEEE/CVF Conference on Computer Vision and Pattern Recognition*, pages 7210–7219, 2021. [2](#)
- [27] Ben Mildenhall, Pratul P Srinivasan, Matthew Tancik, Jonathan T Barron, Ravi Ramamoorthi, and Ren Ng. Nerf: Representing scenes as neural radiance fields for view synthesis. In *Computer Vision—ECCV 2020: 16th European Conference, Glasgow, UK, August 23–28, 2020, Proceedings, Part I*, pages 405–421, 2020. [1](#), [2](#), [3](#), [6](#), [16](#)

- [28] Ben Mildenhall, Peter Hedman, Ricardo Martin-Brualla, Pratul P Srinivasan, and Jonathan T Barron. Nerf in the dark: High dynamic range view synthesis from noisy raw images. In *Proceedings of the IEEE/CVF Conference on Computer Vision and Pattern Recognition*, pages 16190–16199, 2022. **2**
- [29] Michael Niemeyer, Jonathan T Barron, Ben Mildenhall, Mehdi SM Sajjadi, Andreas Geiger, and Noha Radwan. Regnerf: Regularizing neural radiance fields for view synthesis from sparse inputs. In *Proceedings of the IEEE/CVF Conference on Computer Vision and Pattern Recognition*, pages 5480–5490, 2022. **2**
- [30] Jeongtaek Oh, Jaeyoung Chung, Dongwoo Lee, and Kyoung Mu Lee. Deblurbs: Gaussian splatting for camera motion blur. *arXiv preprint arXiv:2404.11358*, 2024. **6, 14, 15, 16**
- [31] Keunhong Park, Utkarsh Sinha, Jonathan T Barron, Sofien Bouaziz, Dan B Goldman, Steven M Seitz, and Ricardo Martin-Brualla. Nerfies: Deformable neural radiance fields. In *Proceedings of the IEEE/CVF International Conference on Computer Vision*, pages 5865–5874, 2021. **2, 5**
- [32] Keunhong Park, Utkarsh Sinha, Peter Hedman, Jonathan T Barron, Sofien Bouaziz, Dan B Goldman, Ricardo Martin-Brualla, and Steven M Seitz. Hypernerf: A higher-dimensional representation for topologically varying neural radiance fields. *arXiv preprint arXiv:2106.13228*, 2021. **2**
- [33] Sunghyun Park, Kangyeol Kim, Junsoo Lee, Jaegul Choo, Joonseok Lee, Sookyoung Kim, and Edward Choi. Vid-ode: Continuous-time video generation with neural ordinary differential equation. In *Proceedings of the AAAI Conference on Artificial Intelligence*, pages 2412–2422, 2021. **3**
- [34] Naama Pearl, Tali Treibitz, and Simon Korman. Nan: Noise-aware nerfs for burst-denoising. In *Proceedings of the IEEE/CVF Conference on Computer Vision and Pattern Recognition*, pages 12672–12681, 2022. **2**
- [35] Cheng Peng and Rama Chellappa. Pdrf: progressively deblurring radiance field for fast scene reconstruction from blurry images. In *Proceedings of the AAAI Conference on Artificial Intelligence*, pages 2029–2037, 2023. **2, 3, 6, 16**
- [36] Cheng Peng, Yutao Tang, Yifan Zhou, Nengyu Wang, Xijun Liu, Deming Li, and Rama Chellappa. Bags: Blur agnostic gaussian splatting through multi-scale kernel modeling. *arXiv preprint arXiv:2403.04926*, 2024. **2, 3, 6, 7, 8, 15, 16**
- [37] Sida Peng, Junting Dong, Qianqian Wang, Shangzhan Zhang, Qing Shuai, Xiaowei Zhou, and Hujun Bao. Animatable neural radiance fields for modeling dynamic human bodies. In *Proceedings of the IEEE/CVF International Conference on Computer Vision*, pages 14314–14323, 2021. **2**
- [38] Albert Pumarola, Enric Corona, Gerard Pons-Moll, and Francesc Moreno-Noguer. D-nerf: Neural radiance fields for dynamic scenes. In *Proceedings of the IEEE/CVF Conference on Computer Vision and Pattern Recognition*, pages 10318–10327, 2021. **2**
- [39] Olinde Rodrigues. *De l’attraction des sphéroïdes, Correspondence sur l’É-côle Impériale Polytechnique*. PhD thesis, PhD thesis, Thesis for the Faculty of Science of the University of Paris, 1816. **5**
- [40] Yulia Rubanova, Ricky TQ Chen, and David K Duvenaud. Latent ordinary differential equations for irregularly-sampled time series. *Advances in neural information processing systems*, 32, 2019. **3**
- [41] Johannes L Schönberger, Enliang Zheng, Jan-Michael Frahm, and Marc Pollefeys. Pixelwise view selection for unstructured multi-view stereo. In *European conference on computer vision*, pages 501–518. Springer, 2016. **3, 6**
- [42] Otto Seiskari, Jerry Ylilammi, Valtteri Kaatrasalo, Pekka Rantalankila, Matias Turkulainen, Juho Kannala, and Arno Solin. Gaussian splatting on the move: Blur and rolling shutter compensation for natural camera motion, 2024. **8**
- [43] Qi Shan, Jiaya Jia, and Aseem Agarwala. High-quality motion deblurring from a single image. *Acm transactions on graphics (tog)*, 27(3):1–10, 2008. **3, 6**
- [44] Hyeongseok Son, Junyong Lee, Jonghyeop Lee, Sunghyun Cho, and Seungyong Lee. Recurrent video deblurring with blur-invariant motion estimation and pixel volumes. *ACM Transactions on Graphics (TOG)*, 40(5):1–18, 2021. **8**
- [45] Pratul P Srinivasan, Ren Ng, and Ravi Ramamoorthi. Light field blind motion deblurring. In *Proceedings of the IEEE Conference on Computer Vision and Pattern Recognition*, pages 3958–3966, 2017. **3**
- [46] Jiaming Sun, Yiming Xie, Linghao Chen, Xiaowei Zhou, and Hujun Bao. Neuralrecon: Real-time coherent 3d reconstruction from monocular video. In *Proceedings of the IEEE/CVF Conference on Computer Vision and Pattern Recognition*, pages 15598–15607, 2021. **2**
- [47] Edgar Tretschk, Ayush Tewari, Vladislav Golyanik, Michael Zollhöfer, Christoph Lassner, and Christian Theobalt. Non-rigid neural radiance fields: Reconstruction and novel view synthesis of a dynamic scene from monocular video. In *Proceedings of the IEEE/CVF International Conference on Computer Vision*, pages 12959–12970, 2021. **2**
- [48] Guangcong Wang, Zhaoxi Chen, Chen Change Loy, and Ziwei Liu. Sparsenerf: Distilling depth ranking for few-shot novel view synthesis. In *Proceedings of the IEEE/CVF International Conference on Computer Vision*, pages 9065–9076, 2023. **2**
- [49] Jiepeng Wang, Peng Wang, Xiaoxiao Long, Christian Theobalt, Taku Komura, Lingjie Liu, and Wenping Wang. Neuris: Neural reconstruction of indoor scenes using normal priors. In *European Conference on Computer Vision*, pages 139–155. Springer, 2022. **2**
- [50] Peng Wang, Lingjie Liu, Yuan Liu, Christian Theobalt, Taku Komura, and Wenping Wang. Neus: Learning neural implicit surfaces by volume rendering for multi-view reconstruction. *arXiv preprint arXiv:2106.10689*, 2021. **2**
- [51] Peng Wang, Lingzhe Zhao, Ruijie Ma, and Peidong Liu. Bad-nerf: Bundle adjusted deblur neural radiance fields. In *Proceedings of the IEEE/CVF Conference on Computer Vision and Pattern Recognition*, pages 4170–4179, 2023. **2, 3, 6, 16**
- [52] Zirui Wang, Shangzhe Wu, Weidi Xie, Min Chen, and Victor Adrian Prisacariu. Nerf-: Neural radiance fields without known camera parameters. *arXiv preprint arXiv:2102.07064*, 2021. **2**

- [53] Chung-Yi Weng, Brian Curless, Pratul P Srinivasan, Jonathan T Barron, and Ira Kemelmacher-Shlizerman. Humannerf: Free-viewpoint rendering of moving people from monocular video. In *Proceedings of the IEEE/CVF conference on computer vision and pattern Recognition*, pages 16210–16220, 2022. [2](#)
- [54] Oliver Whyte, Josef Sivic, Andrew Zisserman, and Jean Ponce. Non-uniform deblurring for shaken images. *International journal of computer vision*, 98:168–186, 2012. [3](#)
- [55] Jamie Wynn and Daniyar Turmukhambetov. Diffusionerf: Regularizing neural radiance fields with denoising diffusion models. In *Proceedings of the IEEE/CVF Conference on Computer Vision and Pattern Recognition*, pages 4180–4189, 2023. [2](#)
- [56] Jiawei Yang, Marco Pavone, and Yue Wang. Freenerf: Improving few-shot neural rendering with free frequency regularization. In *Proceedings of the IEEE/CVF Conference on Computer Vision and Pattern Recognition*, pages 8254–8263, 2023. [2](#)
- [57] Wang Yifan, Felice Serena, Shihao Wu, Cengiz Öztireli, and Olga Sorkine-Hornung. Differentiable surface splatting for point-based geometry processing. *ACM Transactions on Graphics (TOG)*, 38(6):1–14, 2019. [3](#)
- [58] Alex Yu, Ruilong Li, Matthew Tancik, Hao Li, Ren Ng, and Angjoo Kanazawa. Plenotrees for real-time rendering of neural radiance fields. In *Proceedings of the IEEE/CVF International Conference on Computer Vision*, pages 5752–5761, 2021. [2](#)
- [59] Zehao Yu, Anpei Chen, Binbin Huang, Torsten Sattler, and Andreas Geiger. Mip-splatting: Alias-free 3d gaussian splatting. In *Proceedings of the IEEE/CVF Conference on Computer Vision and Pattern Recognition*, pages 19447–19456, 2024. [2](#), [6](#), [7](#), [12](#)
- [60] Syed Waqas Zamir, Aditya Arora, Salman Khan, Munawar Hayat, Fahad Shahbaz Khan, Ming-Hsuan Yang, and Ling Shao. Multi-stage progressive image restoration. In *Proceedings of the IEEE/CVF conference on computer vision and pattern recognition*, pages 14821–14831, 2021. [6](#), [8](#)
- [61] Lingzhe Zhao, Peng Wang, and Peidong Liu. Bad-gaussians: Bundle adjusted deblur gaussian splatting. *arXiv preprint arXiv:2403.11831*, 2024. [2](#), [3](#), [6](#), [7](#), [12](#), [15](#), [16](#)

Appendix

A. Implementation Details

CRiM-GS is trained for 40k iterations based on Mip-Splatting [59]. We set the number of poses N that constitute the continuous camera trajectory to 9. The embedding function of Sec. 4.2 is implemented by `nn.Embedding` of PyTorch, and the embedded features have the sizes of hidden state of 64. In addition, the sizes of hidden state of the encoders \mathcal{E}_r , \mathcal{E}_c , and the decoders \mathcal{D}_r , \mathcal{D}_c are also 64. The neural derivative function f consists of two parallel single linear layers, where one is designated for the rotation matrix and the other for the translation vector. To ensure nonlinearity in the camera motion within the latent space, we apply the ReLU activation function to each layer. The structure of g is identical to that of f . The CNN \mathcal{F} consists of three convolutional layers with 64 channels with kernel size of 5×5 for the first layer and 3×3 for the rest ones. The pixel-wise weights are obtained by applying a pointwise convolutional layer, and the scalar mask \mathcal{M} is obtained by applying another pointwise convolution to the output of \mathcal{F} and averaging it to the batch axis. For first 1k iterations, Gaussian primitives are roughly trained without rigid body transformation and adaptive distortion-aware transformation. After 1k iterations, those transformations start to be trained without the pixel-wise weight and the scalar mask to allow the initial camera motion path to be sufficiently optimized. After 3k iterations, the pixel-wise weight and the scalar mask start training. We set λ_c , λ_o , and $\lambda_{\mathcal{M}}$ to 0.3, 10^{-4} , and 10^{-3} respectively for the objective function. All experiments are conducted on a single NVIDIA RTX 3090 GPU.

B. Additional Ablation Study

Neural ODE for Camera Motion. We conducted a series of ablative experiments on the neural ODE [5] structure of CRiM-GS and the results are shown in Tab. 3. Note that all experiments, except for those involving splines, incorporate both rigid body transformation and adaptive distortion-aware transformation.

The first approach explores representing the camera motion trajectory using splines in $SE(3)$ space instead of neural ODE. This is the primary contribution of BAD-Gaussian [61], and thus, the spline experiment results in Tab. 3 correspond to the performance of BAD-Gaussian. Since BAD-Gaussian assumes very short exposure times, it effectively captures simple camera movements but tends to oversimplify the trajectory when the camera motion becomes nonlinear due to the longer exposure time. In contrast, the our structure assumes more complex camera motion, providing a more comprehensive representation.

The second approach replaces the sequential modeling of

Table 3. Structural ablation for neural ODE for camera motion. “-P” and “-L” denote modeling in the physical space and latent space, respectively.

Methods	Synthetic Scene Dataset			Real-World Scene Dataset		
	PSNR \uparrow	SSIM \uparrow	LPIPS \downarrow	PSNR \uparrow	SSIM \uparrow	LPIPS \downarrow
Spline [61]	21.12	0.5852	0.1007	20.82	0.5912	0.1000
MLP	29.34	0.8644	0.0784	25.94	0.7845	0.0945
RNN-P	29.11	0.8621	0.0604	25.50	0.7719	0.0877
RNN-L	29.95	0.8881	0.0507	26.78	0.8157	0.0713
Neural ODE-P	29.74	0.8854	0.0542	26.57	0.8221	0.0794
Neural ODE-L	30.44	0.9095	0.0441	27.33	0.8310	0.0634

camera paths via neural ODE with a method using MLP. In this method, the embedded features pass through the encoder and three MLP layers with a hidden state size of 64 to obtain the transformation matrices. However, this approach fails to consider the continuous nature of camera motion, resulting in lower performance compared to other methods.

The third and fourth approaches involve using Recurrent Neural Networks (RNN). In the first RNN-based method, the model directly outputs the physical components of the transformation matrices (*e.g.*, components of screw axis). In the second, similar to the proposed method, the RNN extracts features in the latent space, and the physical components are obtained through a decoder. While the latent RNN performs better than the physical space RNN, both are relatively vulnerable to non-uniform blur, as they apply continuous dynamics uniformly over *the same time steps*.

Our approach, which models the camera trajectory using neural ODE, is robust against most types of camera motion blur, as it applies continuous dynamics over irregular time steps. Furthermore, similar to the RNN-based methods, we conduct ablations on the neural ODE in physical and latent spaces, with results indicating higher performance when implemented in the latent space. When neural ODE is applied in the physical space, the features extracted by the encoder (*i.e.*, initial value $\mathbf{z}(t_0)$) directly correspond to physical meanings. However, the components of the screw axis in the rigid body transformation do not exhibit physical continuity, which is why the neural ODE implementation in the latent space achieves the highest performance.

Number of Poses on Camera Motion We conduct ablation experiments on the number of camera poses composing the continuous camera motion, and the results are shown in Tab. 4. The results indicate that performance improves across all metrics as N increases, suggesting that a larger number of camera poses allows for more precise modeling of the camera motion trajectory. However, beyond $N = 8$, the performance stabilizes and based on these observations, we adopt $N = 9$ as it offers the best overall performance.

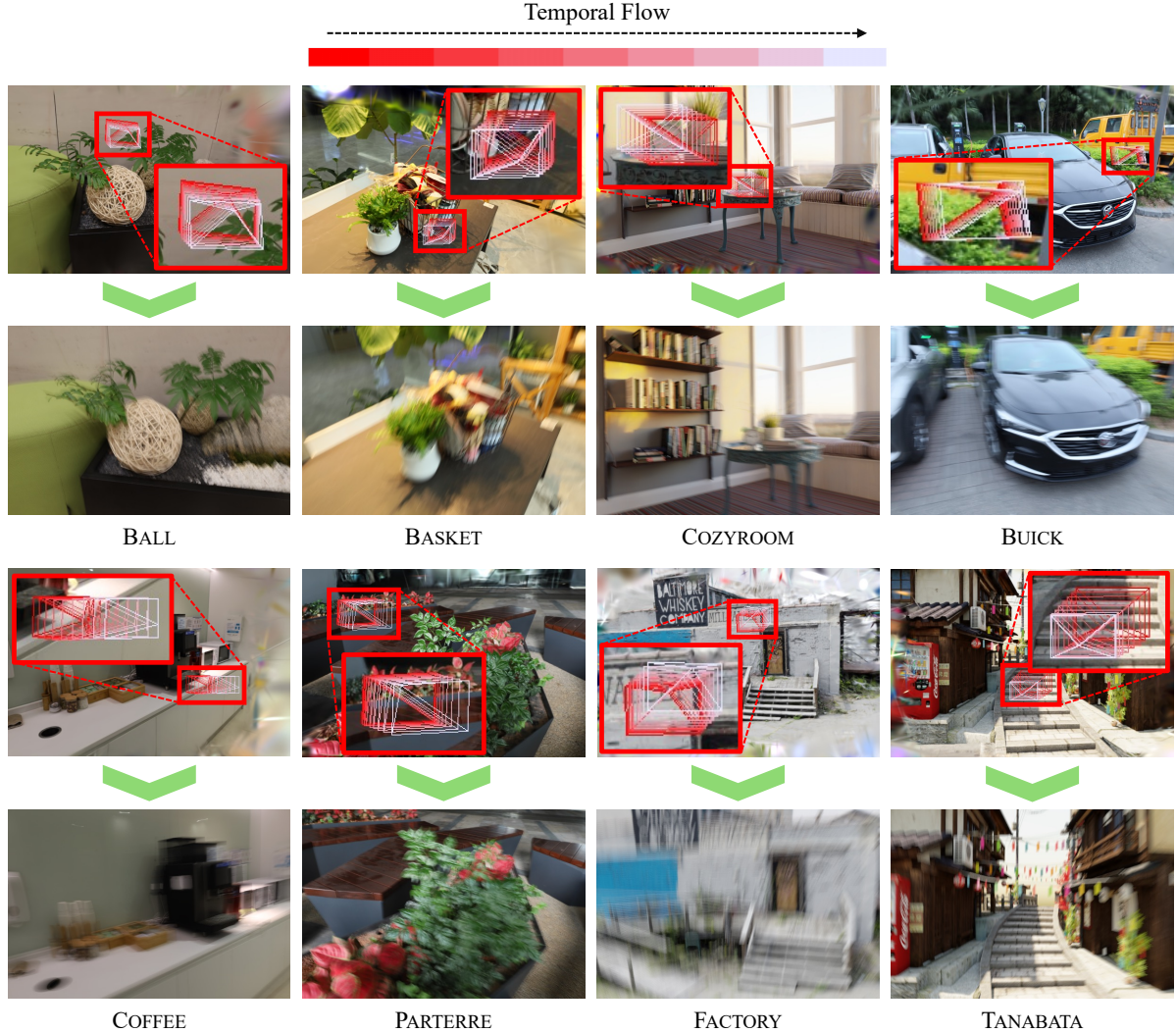


Figure 6. Camera motion trajectory predicted by CRiM-GS for input images with significant blur.

Table 4. Experimental results based on the number of poses N along the camera motion trajectory.

Methods	Synthetic Scene Dataset			Real-World Scene Dataset		
	PSNR \uparrow	SSIM \uparrow	LPIPS \downarrow	PSNR \uparrow	SSIM \uparrow	LPIPS \downarrow
$N=5$	27.40	0.8314	0.0936	26.42	0.8040	0.0924
$N=6$	28.78	0.8610	0.711	26.77	0.8082	0.0822
$N=7$	29.52	0.8758	0.0655	27.01	0.8145	0.0762
$N=8$	30.17	0.9002	0.0501	26.81	0.8101	0.0699
$N=9$	30.44	0.9095	0.0441	27.33	0.8310	0.0634
$N=10$	30.58	0.9124	0.0445	27.12	0.8227	0.0630

C. Difference from SMURF [19]

In this section, we compare our approach with SMURF, a methodology for handling the continuous dynamics of camera motion blur. SMURF utilizes neural ODE to warp a given input ray into continuous rays that simulate cam-

era motion. However, its continuous dynamics are applied only in the 2D pixel space, lacking the inclusion of higher-dimensional camera motion in 3D space. Additionally, as SMURF is implemented on Tensorial Radiance Fields (TensorRF) [4], a ray tracing-based method, it exhibits relatively slower training and rendering speeds.

In contrast, our model uses neural ODE to obtain the 3D camera poses which constitute the camera motion trajectory. Our approach incorporates higher-dimensional information compared to SMURF by operating directly in 3D space rather than the 2D pixel space. Furthermore, as our method is implemented on 3DGS [15], a rasterization-based method, it ensures faster training and rendering speeds than SMURF.

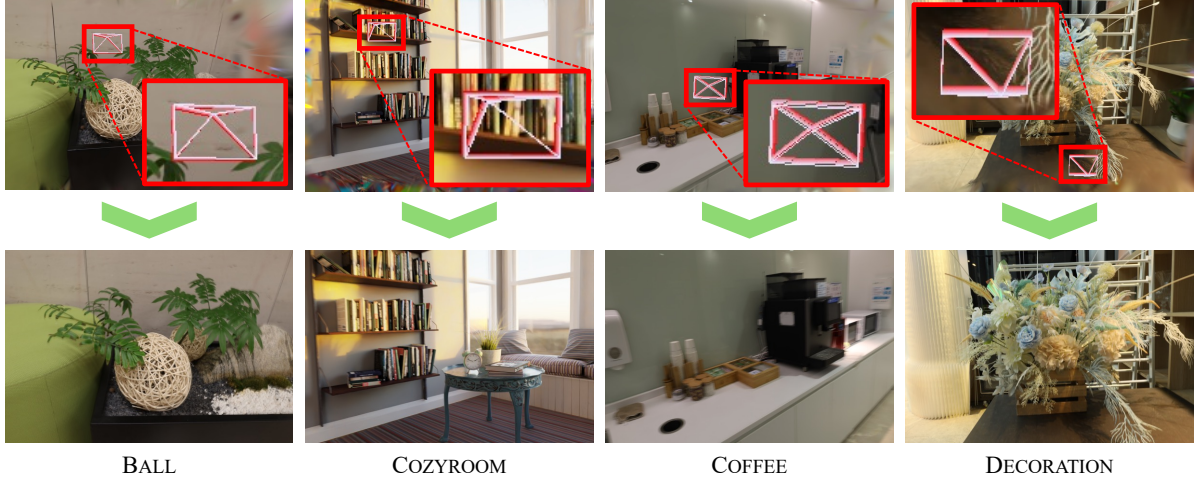


Figure 7. Camera motion trajectory predicted by CRiM-GS for input images with moderate blur.

Table 5. Experimental results based on whether pose optimization is performed after training

Methods	P.O.	Synthetic Scene Dataset			Real-World Scene Dataset		
		PSNR \uparrow	SSIM \uparrow	LPIPS \downarrow	PSNR \uparrow	SSIM \uparrow	LPIPS \downarrow
DeblurGS* [30]		20.22	0.5454	0.1042	20.48	0.5813	0.1186
CRiM-GS		30.44	0.9095	0.0441	27.33	0.8310	0.0634
DeblurGS* [30]	\checkmark	30.24	0.8922	0.0637	26.07	0.8024	0.0958
CRiM-GS	\checkmark	30.65	0.9123	0.0435	28.34	0.8478	0.0606

D. Post-Training Pose Optimization

We reproduce the results of DeblurGS [30] as it performs post-training optimization of test camera poses. This process requires test images and input test camera poses to obtain optimal poses, making it difficult to consider a fair comparison. Nevertheless, as shown in Tab. 5, CRiM-GS achieves better performance with the same pose optimization process as DeblurGS, and even without the post-training optimization, CRiM-GS outperforms the DeblurGS with optimized poses. This indicates that CRiM-GS is robust to inaccurate camera poses. As illustrated in the error maps in Fig. 9, CRiM-GS not only performs better than DeblurGS but also optimizes poses better than other models without additional training.

E. Blur Kernel Visualization

We visualize the camera motion trajectories for input blurry images predicted by CRiM-GS in Fig. 6 and Fig. 7. Fig. 6 illustrates camera motions for images with significant blur, where the predicted trajectories are continuous over time and align precisely with the input images. Fig. 7 depicts camera motions for images with relatively less blur, where

the predicted trajectories show minimal movement, yet still match the input images accurately. These results demonstrate that our blurring kernel effectively models precise continuous camera motion.

F. Derivation of Rigid Body Motion [24]

In this section, we explain the derivation process for Eq. (9) and Eq. (10) from the main paper. This derivation aims to expand and simplify the process described in Modern Robotics [24] for better clarity and accessibility.

The components of a given screw axis include the unit rotation axis $\hat{\omega} \in \mathbb{R}^3$ and the translation component $v \in \mathbb{R}^3$. The unit rotation axis consists of the angular velocity ω and the rotation angle θ :

$$\hat{\omega} = \frac{\omega}{\theta}, \quad \text{where } \|\hat{\omega}\| = 1. \quad (15)$$

We combine the rotation axis $\hat{\omega}$ and the rotation angle θ to represent an element of the Lie Algebra, $\mathfrak{so}(3)$, which serves as the linear approximation of the rotation matrix. Before proceeding, $\hat{\omega}$ is converted into a 3×3 skew-symmetric matrix $[\hat{\omega}]$ to compactly express the cross-product operation as a matrix multiplication:

$$[\hat{\omega}] = \begin{bmatrix} 0 & -\hat{\omega}_z & \hat{\omega}_y \\ \hat{\omega}_z & 0 & -\hat{\omega}_x \\ -\hat{\omega}_y & \hat{\omega}_x & 0 \end{bmatrix} \in \mathfrak{so}(3), \quad \text{where } [\hat{\omega}]^3 = -I. \quad (16)$$

Using the skew-symmetric matrix $[\hat{\omega}]$ and the translation component v , the screw axis $[S]$ is expressed. By multiplying this screw axis with θ , we incorporate the magnitude of the rotation and translation along the screw axis:

$$[S]\theta = \begin{bmatrix} [\hat{\omega}]\theta & v\theta \\ 0 & 0 \end{bmatrix} \in \mathfrak{se}(3), \quad (17)$$

where $\mathfrak{se}(3)$ represents the Lie Algebra, which corresponds to the infinitesimal changes of the Lie Group $SE(3)$. To map this infinitesimal change to the $SE(3)$ transformation matrix $\mathbf{T} = e^{[\mathcal{S}]^\theta}$, we use the Taylor expansion, following these steps:

$$e^{[\mathcal{S}]^\theta} = \sum_{n=0}^{\infty} [\mathcal{S}]^n \frac{\theta^n}{n!} \quad (18)$$

$$= I + [\mathcal{S}]^\theta + [\mathcal{S}]^2 \frac{\theta^2}{2!} + \dots \quad (19)$$

$$= \begin{bmatrix} I + [\hat{\omega}]\theta + [\hat{\omega}]^2 \frac{\theta^2}{2!} + \dots & (I\theta + [\hat{\omega}] \frac{\theta^2}{2!} + \dots) v \\ 0 & 1 \end{bmatrix} \quad (20)$$

$$= \begin{bmatrix} e^{[\hat{\omega}]\theta} & G(\theta)v \\ 0 & 1 \end{bmatrix} \in SE(3) \quad (21)$$

$$\therefore [\mathcal{S}]^n = \begin{bmatrix} [\hat{\omega}]^n & [\hat{\omega}]^{n-1}v \\ 0 & 0 \end{bmatrix} \quad (22)$$

For the rotation matrix $e^{[\hat{\omega}]\theta}$, we simplify it using the Taylor expansion and Eq. (16), resulting in:

$$e^{[\hat{\omega}]\theta} = I + [\hat{\omega}]\theta + [\hat{\omega}]^2 \frac{\theta^2}{2!} + [\hat{\omega}]^3 \frac{\theta^3}{3!} + [\hat{\omega}]^4 \frac{\theta^4}{4!} \dots \quad (23)$$

$$= I + \left(\theta - \frac{\theta^3}{3!} + \dots \right) [\hat{\omega}] + \left(\frac{\theta^2}{2!} - \frac{\theta^4}{4!} + \dots \right) [\hat{\omega}]^2 \quad (24)$$

$$= I + \sin \theta [\hat{\omega}] + (1 - \cos \theta) [\hat{\omega}]^2 \in SO(3) \quad (25)$$

The translational component $G(\theta)$ is also derived using the Taylor expansion and Eq. (16):

$$G(\theta) = I\theta + [\hat{\omega}] \frac{\theta^2}{2!} + [\hat{\omega}]^2 \frac{\theta^3}{3!} + [\hat{\omega}]^3 \frac{\theta^4}{4!} + \dots \quad (26)$$

$$= I\theta + \left(\frac{\theta^2}{2!} - \frac{\theta^4}{4!} + \dots \right) [\hat{\omega}] + \left(\frac{\theta^3}{3!} - \frac{\theta^5}{5!} + \dots \right) [\hat{\omega}]^2 \quad (27)$$

$$= I\theta + (1 - \cos \theta) [\hat{\omega}] + (\theta - \sin \theta) [\hat{\omega}]^2 \quad (28)$$

The term $G(\theta)$ physically represents the total translational motion caused by the rotational motion as the rigid body rotates by θ . In other words, $G(\theta)$ indicates how rotational motion contributes to translational motion, which can also be expressed as an integral of the rotation motion:

$$G(\theta) = \int_0^\theta e^{[\hat{\omega}]^\theta} d\theta \quad (29)$$

$$= \int_0^\theta (I + \sin \theta [\hat{\omega}] + (1 - \cos \theta) [\hat{\omega}]^2) d\theta \quad (30)$$

$$= I\theta + (1 - \cos \theta) [\hat{\omega}] + (\theta - \sin \theta) [\hat{\omega}]^2 \quad (31)$$

Through the above process, we derive Eq. (9) and Eq. (10) in the main paper, improving readability of the paper and providing a clear foundation for understanding the mathematical framework.

G. Per-Scene Quantitative Results

We show the per-scene quantitative performance on synthetic and real-world datasets in Tab. 7 and Tab. 6. CRiM-GS demonstrates superior performance on most scenes in the real-world dataset and achieves the highest performance across all scenes in the synthetic dataset. Notably, CRiM-GS achieves the best LPIPS scores for all scenes, highlighting the superior quality achieved by our CRiM-GS.

H. Additional Qualitative Results

We provide additional visualization results in Fig. 8, which demonstrate that our CRiM-GS outperforms not only in quantitative metrics but also in qualitative performance. For comparative videos, please refer to *the supplementary materials*.

Error Map Visualization. We extract error maps for three scenes to enable direct comparison with other methods, and the results are shown in Fig. 9. While BAD-Gaussians [61] and DeblurGS [30] exhibit relatively high errors, BAGS [36] and CRiM-GS demonstrate lower errors. Notably, our model captures the overall contours of the scene more effectively than BAGS.

I. Limitation

Despite achieving superior qualitative and quantitative performance with fast rendering, the proposed model faces room for optimization in terms of training efficiency. The primary challenge lies in the multiple rendering steps per iteration and the use of the CNN module \mathcal{F} for pixel-wise weighted sums, which is employed only during training. However, this aspect offers opportunities for future improvements. Designing continuous motion directly at the 3D Gaussian level could streamline the process, reducing training time without compromising performance.

Table 6. Per-Scene Quantitative Performance on the Real-World Scenes.

Real-World Scene	BALL			BASKET			BUICK			COFFEE			DECORATION		
	PSNR↑	SSIM↑	LPIPS↓	PSNR↑	SSIM↑	LPIPS↓	PSNR↑	SSIM↑	LPIPS↓	PSNR↑	SSIM↑	LPIPS↓	PSNR↑	SSIM↑	LPIPS↓
Naive NeRF [27]	24.08	0.6237	0.3992	23.72	0.7086	0.3223	21.59	0.6325	0.3502	26.48	0.8064	0.2896	22.39	0.6609	0.3633
Deblur-NeRF [25]	27.36	0.7656	0.2230	27.67	0.8449	0.1481	24.77	0.7700	0.1752	30.93	0.8981	0.1244	24.19	0.7707	0.1862
PDRF-10* [35]	27.37	0.7642	0.2093	28.36	0.8736	0.1179	25.73	0.7916	0.1582	31.79	0.9002	0.1133	23.55	0.7508	0.2145
BAD-NeRF* [51]	21.33	0.5096	0.4692	26.44	0.8080	0.1325	21.63	0.6429	0.2593	28.98	0.8369	0.1956	22.13	0.6316	0.2894
DP-NeRF [18]	27.20	0.7652	0.2088	27.74	0.8455	0.1294	25.70	0.7922	0.1405	31.19	0.9049	0.1002	24.31	0.7811	0.1639
DeblurGS [30]	21.44	0.5760	0.1480	21.00	0.6706	0.0908	18.91	0.5539	0.1442	25.97	0.8299	0.0614	19.60	0.5713	0.1035
BAD-Gaussians* [61]	22.14	0.5791	0.1095	21.48	0.6787	0.0603	18.81	0.5271	0.0952	24.54	0.7627	0.1031	20.30	0.6162	0.0881
Deblurring 3DGS [17]	28.27	0.8233	0.1413	28.42	0.8713	0.1155	25.95	0.8367	0.0954	32.84	0.9312	0.0676	25.87	0.8540	0.0933
BAGS [36]	27.68	0.7990	0.1500	29.54	0.9000	0.0680	26.18	0.8440	0.0880	31.59	0.9080	0.0960	26.09	0.8580	0.0830
CRiM-GS	28.25	0.8064	0.1074	30.85	0.9048	0.0425	26.51	0.8379	0.0585	32.26	0.9230	0.0421	26.34	0.8610	0.0569
Real-World Scene	GIRL			HERON			PARTERRE			PUPPET			STAIR		
	PSNR↑	SSIM↑	LPIPS↓	PSNR↑	SSIM↑	LPIPS↓	PSNR↑	SSIM↑	LPIPS↓	PSNR↑	SSIM↑	LPIPS↓	PSNR↑	SSIM↑	LPIPS↓
Naive NeRF [27]	20.07	0.7075	0.3196	20.50	0.5217	0.4129	23.14	0.6201	0.4046	22.09	0.6093	0.3389	22.87	0.4561	0.4868
Deblur-NeRF [25]	22.27	0.7976	0.1687	22.63	0.6874	0.2099	25.82	0.7597	0.2161	25.24	0.7510	0.1577	25.39	0.6296	0.2102
PDRF-10* [35]	24.12	0.8328	0.1679	22.53	0.6880	0.2358	25.36	0.7601	0.2263	25.02	0.7496	0.1532	25.20	0.6235	0.2288
BAD-NeRF* [51]	18.10	0.5652	0.3933	22.18	0.6479	0.2226	23.44	0.6243	0.3151	22.48	0.6249	0.2762	21.52	0.4237	0.3341
DP-NeRF [18]	23.33	0.8139	0.1498	22.88	0.6930	0.1914	25.86	0.7665	0.1900	25.25	0.7536	0.1505	25.59	0.6349	0.1772
DeblurGS* [30]	18.28	0.6660	0.1044	18.70	0.4579	0.1488	19.78	0.4953	0.1744	19.50	0.5302	0.1297	21.63	0.4623	0.0808
BAD-Gaussians* [61]	18.72	0.6765	0.0925	18.53	0.4498	0.1412	20.79	0.5589	0.1298	21.08	0.6036	0.1022	21.77	0.4640	0.0782
Deblurring 3DGS [17]	23.26	0.8390	0.1011	23.14	0.7438	0.1543	26.17	0.8144	0.1206	25.67	0.8051	0.0941	26.46	0.7050	0.1123
BAGS [36]	25.45	0.8690	0.0790	22.04	0.7150	0.1260	25.92	0.8190	0.0920	25.81	0.8040	0.0940	26.69	0.7210	0.0800
CRiM-GS	26.20	0.8780	0.0438	22.84	0.7234	0.1110	26.09	0.8126	0.0698	26.66	0.8236	0.0613	27.30	0.7390	0.0415

Table 7. Per-Scene Quantitative Performance on the Synthetic Scenes.

Synthetic Scene	FACTORY			COZYROOM			POOL			TANABATA			TROLLEY		
	PSNR↑	SSIM↑	LPIPS↓	PSNR↑	SSIM↑	LPIPS↓	PSNR↑	SSIM↑	LPIPS↓	PSNR↑	SSIM↑	LPIPS↓	PSNR↑	SSIM↑	LPIPS↓
Deblur-NeRF [25]	25.60	0.7750	0.2687	32.08	0.9261	0.0477	31.61	0.8682	0.1246	27.11	0.8640	0.1228	27.45	0.8632	0.1363
PDRF-10* [35]	25.87	0.8316	0.1915	31.13	0.9225	0.0439	31.00	0.8583	0.1408	28.01	0.8931	0.1004	28.29	0.8921	0.0931
BAD-NeRF* [51]	24.43	0.7274	0.2134	29.77	0.8864	0.0616	31.51	0.8620	0.0802	25.32	0.8081	0.1077	25.58	0.8049	0.1008
DP-NeRF [18]	25.91	0.7787	0.2494	32.65	0.9317	0.0355	31.96	0.8768	0.0908	27.61	0.8748	0.1033	28.03	0.8752	0.1129
DeblurGS* [30]	17.82	0.3980	0.1453	22.88	0.6758	0.0514	24.53	0.6095	0.1171	17.54	0.4800	0.1132	18.32	0.5638	0.0942
BAD-Gaussians* [61]	16.84	0.3220	0.2425	22.31	0.6954	0.0519	26.70	0.7051	0.0642	20.13	0.6095	0.0729	19.60	0.5941	0.0722
Deblurring 3DGS [17]	24.01	0.7333	0.2326	31.45	0.9222	0.0367	31.87	0.8829	0.0751	27.01	0.8807	0.0785	26.88	0.8710	0.1028
BAGS [36]	22.35	0.6639	0.2277	32.21	0.9359	0.0245	28.72	0.8404	0.0804	26.79	0.8735	0.1099	26.61	0.8627	0.1156
CRiM-GS	28.72	0.8874	0.0604	33.01	0.9409	0.0209	32.05	0.8882	0.0524	29.04	0.9180	0.0376	29.36	0.9131	0.0492

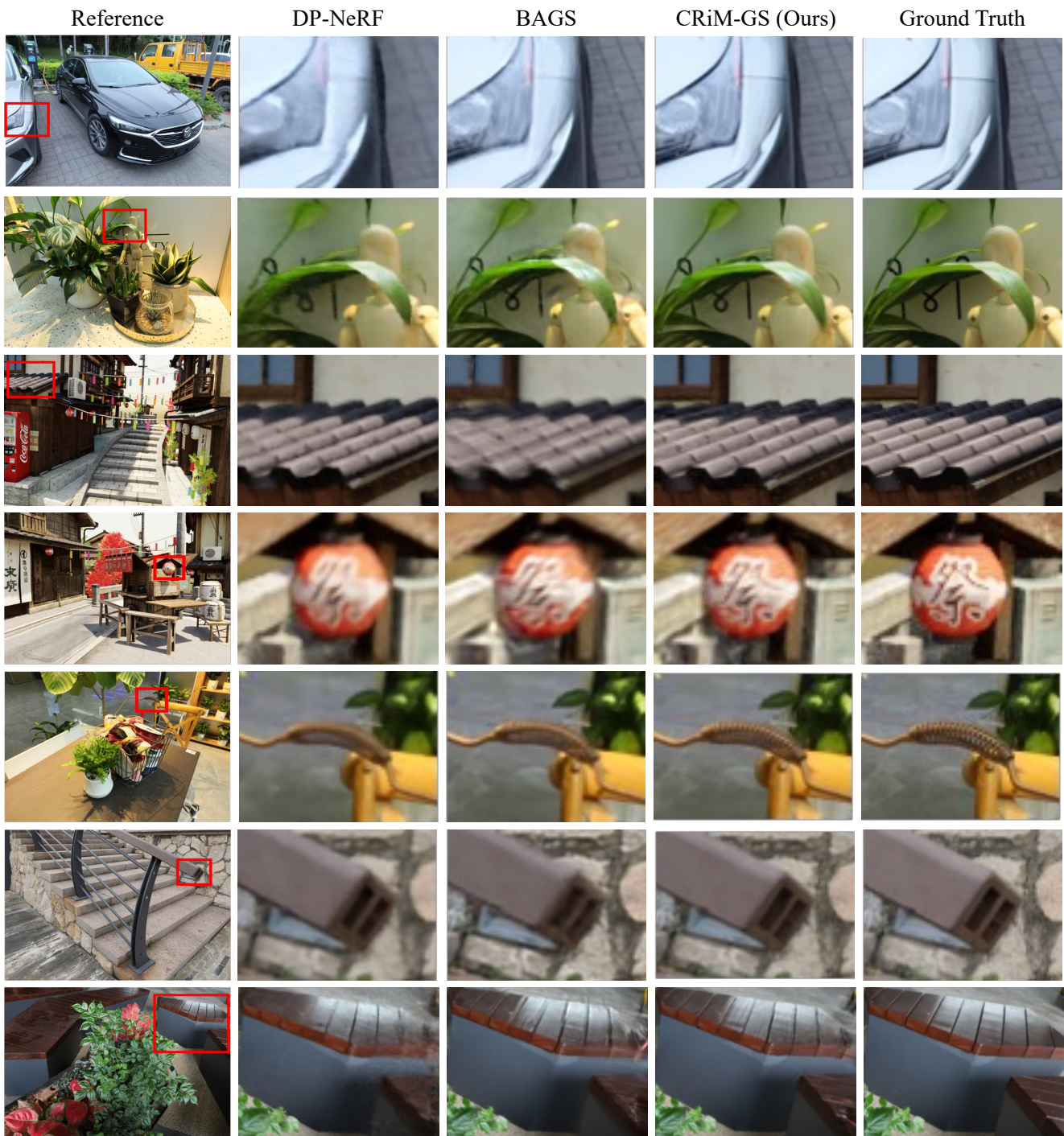


Figure 8. Additional Qualitative Comparison on the Synthetic and Real-World Scenes.

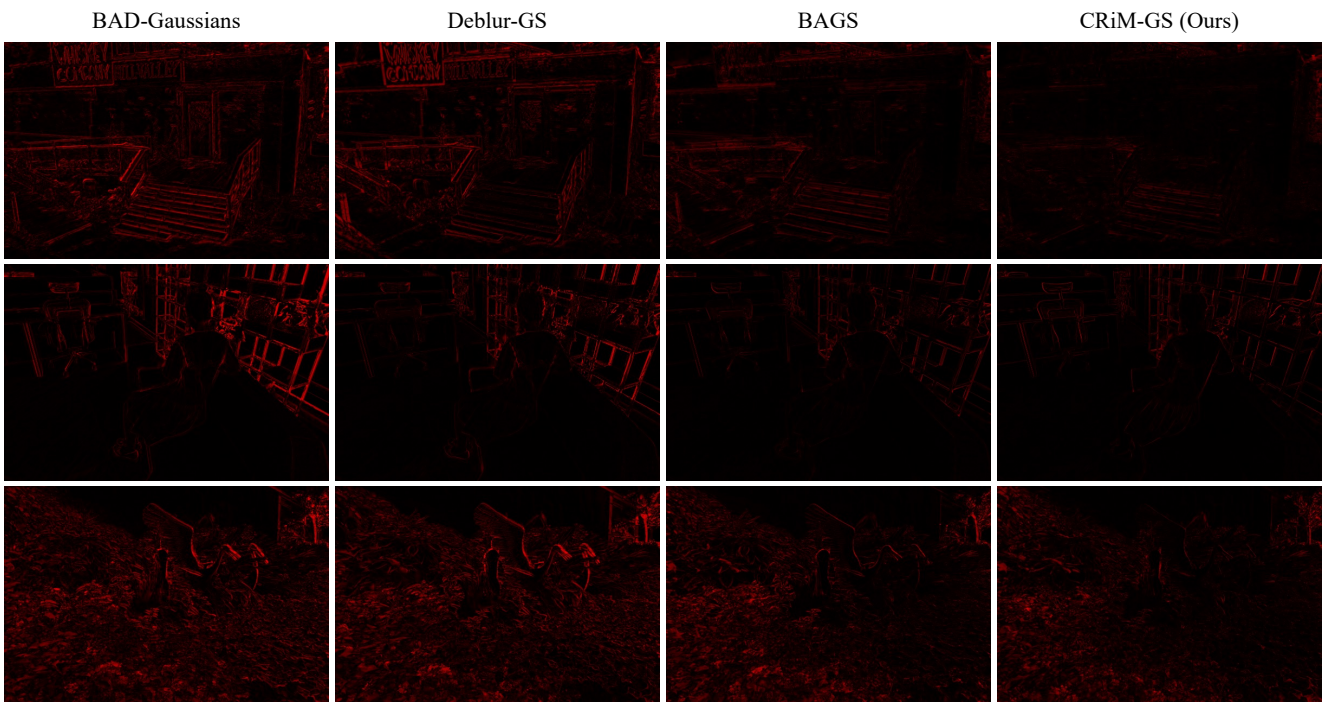


Figure 9. Error Map Comparison.